www.sciencemag.org/cgi/content/full/science.aad6004/DC1

Supplementary Materials for

Observation of the ^{60}Fe nucleosynthesis-clock isotope in galactic cosmic rays

W. R. Binns,* M. H. Israel,* E. R. Christian, A. C. Cummings, G. A. de Nolfo, K. A. Lave, R. A. Leske, R. A. Mewaldt, E. C. Stone, T. T. von Rosenvinge, M. E. Wiedenbeck

*Corresponding author: Email: wrb@wustl.edu (W.R.B.); mhi@wustl.edu (M.H.I.)

Published 21 April 2016 on *Science* First Release
DOI: 10.1126/science.aad6004

This PDF file includes:

Materials and Methods

Method

The data were selected as follows. Cosmic-ray events were analyzed if they stopped in ranges E4 through E8 (see Figure 1A). This allowed us to make between three and seven measurements of dE/dx and the residual energy (E_{Res}), depending upon the range in which they stopped. Most particles that interact within the instrument are rejected because one of the products of the interaction gives a signal in the penetration counter (E9) or one of the guard counters. For the small fraction of interacted particles remaining, we require that estimates of charge from these multiple measurements, which are closely related to the mass estimate, agree. Specifically we require that the root-mean-square deviation from the mean of these charge estimates (z_{rms}, see Figure S1) be <0.1 e. In Figure S1 we show the dependence of the ^{60}Fe/Fe ratio as a function of z_{rms}. As the z_{rms} cut is reduced from 0.30, the ratio declines slightly, leveling off at z_{rms} <0.15. We have chosen the cut value of 0.10 since it shows slightly better separation between the ^{58}Fe tail and the ^{60}Fe events, while retaining good statistics. Particles were selected for their trajectory angle < 30º, measured from the normal to the surfaces of the silicon detectors. The silicon detector wafers have dead layers with typical thicknesses ~55-70 μm on one surface (*5*). Because the shapes of the measured ΔE versus residual energy tracks for particles that stop close to the dead layers are significantly altered from those expected with no dead layers, we restrict the analysis to particles that stop at depths in the residual-energy detector that are at least 500 μm from the detector surface exhibiting the dead layers, as calculated from the measured energy deposit and the angle of incidence using a range-energy relation.

There are quality requirements on the trajectory as determined by the hodoscope, and the trajectory must traverse the silicon and fiber-trigger detectors > 1mm inside the active regions. Events collected over the time interval extending from 4 December 1997 to 27 September 2014 were analyzed. A total of 5800 days were analyzed and 342 days were eliminated because of elevated solar energetic particle activity.

Supplementary Text

Results: Tests of ^{60}Fe Events

We have performed a number of tests on the ^{60}Fe events to verify that they are not anomalous in any way relative to other Fe events.

We find that the distributions in particle trajectory angle with respect to the instrument normal for ^{60}Fe and Fe are similar (Fig. S2A & B). The six ^{60}Fe particles in the "clump" centered at 22-23º do not appear to be special in any way. We believe it is just a result of statistics of small numbers.

We have also compared the distributions in time of detection for Fe (Fig. S3A) and ^{60}Fe (Fig. S3B), for the days covered by this analysis. In that figure, "Day of Year

(DOY96)" begins on 1 January 1996. The data set presented here begins on DOY96 704 and ends on DOY96 6845, corresponding to 4 December 1997 and 27 September 2014 respectively. We find these distributions are also similar.

The number of events stopping in each of the detectors E4 through E8 is shown for Fe and ^{60}Fe in Fig. S4A and S4B respectively. Again, the distributions are very similar.

The "margin" of the silicon detectors is defined as the distance from the penetration point of the particle to the sensitive area edge of the detector. Figs. S5A, B, and C give the distribution in this quantity for ^{56}Fe for three silicon detectors E1, E2, and E-next (E-next is the detector following the detector in which the particle stops, and the distance from the projected penetration point of that detector to its edge is shown). Figs. S5D, E, and F give the distributions for ^{60}Fe. Clearly the ^{56}Fe and ^{60}Fe distributions are similar.

There are three similar "margins" defined for the trigger fiber plane, which is square, not circular as the silicon detectors are. The "x-fiber margin" is defined as the perpendicular distance between the point of particle penetration to the nearest edge of the trigger fiber x-plane. The "y-fiber margin" is defined similarly. The "trigger fiber margin" is defined as the lesser of the x-fiber margin and y-fiber margin to the nearest edge of the square trigger fiber active area. These quantities are plotted in Figs. S6A, B, and C for ^{56}Fe, and in Figs S6D, E, and F for ^{60}Fe. Again we see that the distributions are very similar.

We also note that most physical processes produce distribution tails on the low side of peaks rather than the high side, as can be seen in the ^{54}Fe and ^{57}Co tails in Figs. 2A &B. These very low level tails (nearly two orders of magnitude below the peak) are likely the result of various physical effects (e.g., neutron stripping or channeling in the silicon detectors) that are not efficiently removed by the data cuts. By contrast, the cutoffs on the high sides of ^{58}Fe and ^{59}Co are sharp. Over the full charge range measured by CRIS, one consistently observes more significant tails on the low side of an isotope distribution than on the high side.

Because the dE/dx versus total-E technique identifies particles using a quantity that is a combination of nuclear charge and mass, there can be an ambiguity between a high-mass isotope of atomic number Z and a low-mass isotope of atomic number Z+1. For cosmic rays in the charge range considered here this is not a serious problem because the isotopes in the overlap region have very short halflives and could only be produced locally in the instrument. The mass histograms shown in Figure 2 correspond to a nominal boundary between Fe and Co. Moving this boundary to slightly higher charge would move two events from the end of the low-mass Co tail to around mass 61.5 in the Fe histogram, still well separated from the 15 events that we identify as ^{60}Fe. Thus we think that only the identification of the one Fe event near mass 60.8 is uncertain as to

whether it is ^{60}Fe or background. This event does not contribute to the contamination estimation of ±1 event.

We conclude that the 15 events we have identified as ^{60}Fe are not a tail on a distribution of the more abundant Fe isotopes. They are nearly all surviving primary cosmic-ray nuclei.

Results: Minor Corrections to Abundance Ratio near Earth

A correction factor to the measured ^{60}Fe/^{56}Fe ratio for the differing interaction probabilities of ^{56}Fe and ^{60}Fe in the instrument was calculated. For this correction, we assume that all particles stopping in a given detector stop halfway through the detector. The cumulative areal density in g/cm^2 (silicon equivalent) that particles penetrate before stopping in a given detector was calculated, including a sec(θ) correction for the mean trajectory angle (θ) of 20º. Interaction lengths for ^{56}Fe and ^{60}Fe (*23*) were used to calculate the interaction correction factors to the top of the instrument for each detector and isotope. The ratio of the sums of the corrected numbers of events for ^{60}Fe and ^{56}Fe then gives the overall interaction correction factor of 1.009.

A correction factor is also required for the differing energy ranges of stopping ^{56}Fe and ^{60}Fe nuclei. The maximum and minimum energies for ^{56}Fe and ^{60}Fe in each detector were calculated using range-energy tables. A polynomial fit to the ^{56}Fe spectrum (*15*)

$$\ln(I) = a + b[\ln(E)-\ln(160)] + c[\ln(E)-\ln(160)]^2$$

where a=-16.965, b=0.5204, c=-0.3989, E is energy (MeV/nucleon), and I is intensity (particles/cm^2·sr·s·MeV/nucleon), was integrated from the minimum to maximum energies for each detector and isotope.

The ratios of integrals for ^{56}Fe and ^{60}Fe were then weighted by the number of stopping events in each detector, giving a weighted mean of 1.042. This is the correction factor for the differing energy bands for ^{56}Fe and ^{60}Fe. Thus the overall correction factor to the ^{60}Fe/^{56}Fe abundance ratio near Earth is 1.051.

Results: Derivation of Ratio at the Accelerator Source

Observations by CRIS of the beta-decay secondary cosmic rays ^{10}Be, ^{26}Al, ^{36}Cl, and ^{54}Mn have been well explained using a simple "leaky-box model" of cosmic-ray propagation in the interstellar medium, characterized by a mean escape time from the Galaxy of τ_{esc} = 15.0 ± 1.6 Myr and an average number density for the interstellar medium in which cosmic rays propagate (assumed to be 90% H and 10% He by number) of n_{H+He}=0.38 ± 0.04 H+He atoms cm^{-3} (*18*).

In the context of a simple leaky-box steady-state galactic propagation model (ignoring interstellar energy loss, which is very similar for all the Fe isotopes), if *Q* represents the abundance at the acceleration source, *N* represents the primary abundance near Earth, and $\tau_{decay60}$, τ_{int}, and τ_{esc}, are lifetimes for radioactive decay, mass-changing

interaction in interstellar space, and escape from the Galaxy (we assume the same τ_{esc} for ^{56}Fe and ^{60}Fe), then

$$Q_{60}/Q_{56} = (N_{60}/N_{56}) \times (\tau_{56}/\tau_{60}) \quad (1)$$
$$\text{where } 1/\tau_{56} = 1/\tau_{esc} + 1/\tau_{int56}$$
$$\text{and } 1/\tau_{60} = 1/\tau_{esc} + 1/\tau_{int60} + 1/\tau_{decay60}$$

The mean lifetime for loss of a cosmic-ray species by nuclear interaction with the interstellar medium is $\tau_{int}=\lambda/(n_{H+He}m_{H+He}v)$, where m_{H+He} is the mean atomic mass of interstellar material (2.17×10^{-24}g/atom), and v is the velocity of the cosmic-ray nuclei. From mass-changing cross-sections (*23*), the interaction mean free paths in interstellar gas (90% H and 10% He by number) are $\lambda_{60} = 2.56$ g/cm^2 and $\lambda_{56} = 2.70$ g/cm^2.

The mean energy at the top of the CRIS instrument for the ^{56}Fe in this data set is 340 MeV/nucleon. The ^{60}Fe in this data set have the same range in the detector system as the ^{56}Fe, so they have a slightly lower mean energy/nucleon at the top of the instrument, 327 MeV/nucleon. These energies observed near 1AU are lower than those in the interstellar medium due to adiabatic deceleration in the expanding solar wind. We estimate this energy loss using a spherically symmetric model of cosmic-ray modulation inside the Solar System (*24*). The change in energy-per-nucleon is given by $\Delta(E/M) = (Z/A)\phi$ (*25*), Z and A are the charge and mass numbers and ϕ is a modulation parameter, which we derived from the measured shape of the Fe energy spectrum for each 27-day Bartels solar rotation throughout the 17-year period. During this time, the value of ϕ varied between ~250 MV and ~1000 MV. The average ϕ over this period, weighted by the number of observed Fe events in each 27-day period was 453 MV, corresponding to an energy loss of 210 MeV/nucleon for ^{56}Fe and 196 MeV/nucleon for ^{60}Fe**.** Thus the mean energies in interstellar space were 550 MeV/nucleon for ^{56}Fe and 523 MeV/nucleon for ^{60}Fe, corresponding to velocities 0.778c and 0.768c. Thus we have $\tau_{int56} = 4.45 \pm 0.47$ Myr, giving $\tau_{56} = 3.43 \pm 0.29$ Myr, and $\tau_{int60} = 4.27 \pm 0.45$ Myr.

The mean lifetime for radioactive decay of ^{60}Fe at rest is 3.78 ± 0.06 Myr (2.62 ± 0.04 Myr /ln2). In the interstellar medium, where the mean energy is 523 MeV/nucleon, the Lorentz factor $\gamma = 1.56$ so $\tau_{decay60} = 5.90 \pm 0.09$ Myr, giving $\tau_{60} = 2.13 \pm 0.11$ Myr.

From equation (1) above, the observed ^{60}Fe/^{56}Fe ratio near Earth, $(4.6 \pm 1.7) \times 10^{-5}$, implies a ^{60}Fe/^{56}Fe ratio at the cosmic-ray acceleration source of $R_A = Q_{60}/Q_{56} = (7.5 \pm 2.9) \times 10^{-5}$.

With the same method, using charge-changing instead of mass-changing cross-sections, we have also estimated the ^{60}Fe/Fe ratio at the cosmic-ray acceleration source, using $\lambda_{Fe} = 2.94$ g/cm^2, and find it to be $Q_{60}/Q_{Fe} = (6.2 \pm 2.4) \times 10^{-5}$. We note that the uncertainty in the ^{56}Fe abundance is much smaller than the statistical uncertainty of ^{60}Fe and does not significantly contribute to that of the ^{60}Fe/^{56}Fe ratio.

Estimates of time between nucleosynthesis and acceleration

In deriving the curves shown in Fig. 3, stellar masses were distributed according to the Salpeter Initial-Mass Function (*26*). Since the isotope yields were not calculated for all initial stellar masses between 12 $M_\odot$ to 120 $M_\odot$ (*3,4*) a linear interpolation between the calculated masses was used. The stellar lifetime before core-collapse was taken from (*16*). The decay of ^{60}Fe was accounted for as follows. The first supernova in the OB association occurred ~3 Myr after association birth and ejected its material into the superbubble. Following that, using time increments of 0.25Myr, new material was injected into the superbubble. The ^{60}Fe that had been previously injected was decayed according to its exponential decay time of 3.78 Myr (halflife 2.62 Myr), and added to the newly injected ^{60}Fe. After each time increment, the ^{60}Fe already in the supperbubble was decayed and added to the newly injected material, and the ^{60}Fe/^{56}Fe ratio was calculated. It was assumed that all stellar outflow and ejecta were injected into the superbubble and were available for acceleration, rather than being drawn into a black hole forming after core-collapse. The blue dotted curve is the ratio derived from the isotope yields for non-rotating stars (*3*), and the red dashed and black curves are derived for non-rotating and rotating stars respectively (*4*). As can be seen, there are substantial differences in the predicted ratios of these modeling calculations resulting from uncertainties in the ^{60}Fe-producing reaction rates and model parameters used in the calculations as discussed by (*27–29*). The GCR acceleration source ratio (black horizontal dashed line) inferred from our measured ratio is compared with the modeling calculations in Fig. 3 (the shaded area indicates the uncertainty).

There is strong evidence from the enhanced abundance of ^{22}Ne relative to ^{20}Ne in cosmic rays compared with its Solar System abundance (*16*, *30*) and from the cosmic-ray element abundances from $_{30}$Zn to $_{40}$Zr (*31*, *32*) that the cosmic-ray source is a mixture of ~20% outflow plus ejecta from massive stars and ~80% old material with Solar-System composition. Since the old material would have no ^{60}Fe, we would expect the ^{60}Fe/^{56}Fe ratio in the massive star material (outflow plus ejecta) to be $R_{MS} = R_A/0.2 = (3.75 \pm 1.5) \times 10^{-4}$, where R_A is the ratio of mixed material that is accelerated, assuming the mix was exactly 20% to 80%. In Fig. 3 R_{MS} is the horizontal red dashed line, with the shaded area indicating the measurement plus modeling uncertainties added in quadrature.

In addition to the uncertainties described above, the 20% mix of massive star outflow plus ejecta with old ISM material is approximate. Best chi-squared fits to the element abundances (*30*, *31*) indicate that mix percentages from roughly 10-25% would be consistent with those data, while the ^{22}Ne/^{20}Ne ratio has been interpreted by (*23*) as $R_A=R_{MS} \times (0.18\pm0.05)$.

We can now calculate an upper limit for the time between nucleosynthesis and cosmic-ray acceleration. The modeling curves in Fig. 3 show that the largest ^{60}Fe/^{56}Fe ratio at any time in the life of an OB association is $R_{MS}= 2.8 \times 10^{-3}$ for the non-rotating C&L model (*4*), and this occurs at a time corresponding to the core-collapse of ~80$M_\odot$ stars. This corresponds to a ratio at acceleration of $R_A=0.2R_{MS}=5.6 \times 10^{-4}$. We then assume no additional material is injected into the superbubble and let the ^{60}Fe decay to the bottom of the error bar on our measured best value of $(7.5 \pm 2.9) \times 10^{-5}$. The time for

this decay is then T=(3.78 Myr) × ln [(5.6 × 10^{-4})/(4.6 × 10^{-5})] = 9.4 Myr. If instead we take the peak ^{60}Fe/^{56}Fe ratio from the W&H model (*3*) (Fig. 3), performing the same calculation gives an upper limit of T=(3.78 Myr) × ln [(9 × 10^{-5})/(4.6 × 10^{-5})]= 2.5 Myr.

This approach leaves out several factors that could increase R_{MS}. First, the assumed 80%/20% mix is approximate, as mentioned above. In fact, Murphy (*33*) finds a best fit of 13% $^{+8\%}_{-5\%}$ for ordering of refractory and volatile element abundances with mass. If we were to use a 90%/10% mix, R_{MS} would be a factor of two larger. The second is that from a diffusion standpoint, owing to its radioactive decay, the distance that ^{60}Fe can travel by diffusion is shorter than for a stable nuclide such as ^{56}Fe. This would further increase R_{MS}. Both of these factors will shorten the derived time between nucleosynthesis and acceleration. The time that we presented above is an upper limit. A third factor that is harder to characterize is related to the choice of parameters in the models, such as the mass cut, and the question of the mass range for which black holes are formed directly or by fallback, limiting the ejecta and thus affecting such things as the ^{60}Fe/^{56}Fe ratio.

So we see that the calculated upper limit depends strongly on the assumed nucleosynthesis model. However, since the first upper limit calculated from the non-rotating C&L model is rather extreme, it is likely that the time between nucleosynthesis and acceleration does not exceed a few million years.

Another approach is to look at the cross-over points for the three model curves with the lower error bar for R_{MS} =2.25 × 10^{-4} in Fig. 3. On the low side, the W&H model curve crosses at a time of ~9 Myr, although it is not much below the lower limit for several more Myr. The cross-over point corresponds to a time of ~6 Myr after the first core-collapse. On the high side, the C&L rotating model curve crosses R_{MS} at about 11.1 Myr, ~8 Myr after the first core-collapse. Again we see that the time between nucleosynthesis and acceleration is likely of order a few million years.

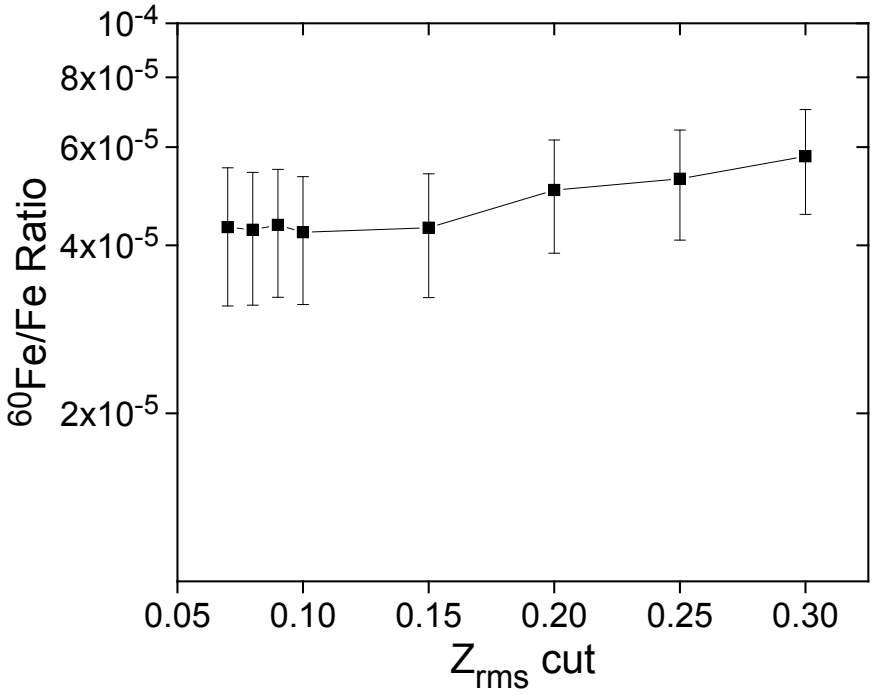

Fig. S1.
^{60}Fe/Fe ratio as a function of a charge estimate consistency selection. We make multiple estimates of the charge for each particle using different combinations of detectors for dE/dx and residual energy (see text). Using these multiple estimates, we calculate the root-mean-square deviation from the mean (z_{rms}) for each event and select events with z_{rms} less than a given value. We see in this plot that the ^{60}Fe/Fe ratio is essentially unchanged for $z_{rms}<0.15$. We have used a cut of 0.10 for the data presented in this paper. Note that the value of the ratio plotted in the figure for $z_{rms} = 0.10$, $(4.2\pm1.1) \times 10^{-5}$, differs from the "abundance ratio at Earth" presented in the main text since here we use all 15 events instead of the 13 used for the corrected abundance determination.

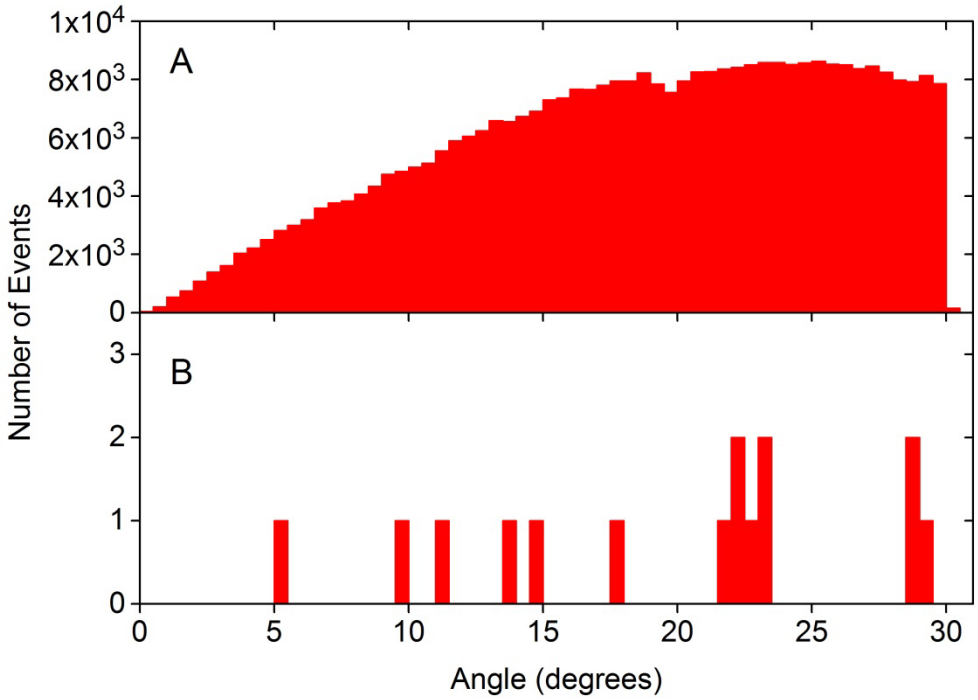

Fig. S2

Trajectory angle distributions for Fe and ^{60}Fe nuclei. The distributions of trajectory angle relative to the normal to the detectors is plotted for **A**) all Fe nuclei and **B**) ^{60}Fe nuclei. We have applied a Kolmogorov-Smirnov (K-S) statistical test to these distributions and obtain an asymptotic probability (p) of 0.56. Therefore the Fe and ^{60}Fe angle distributions are not statistically different.

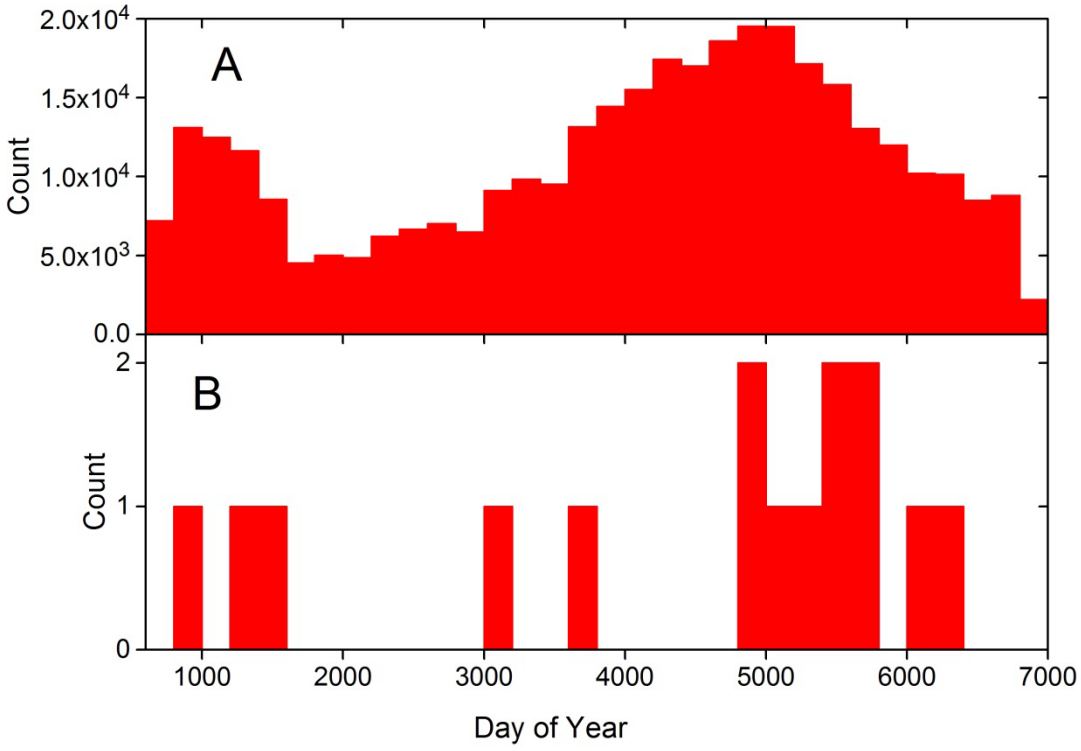

Fig. S3

Distributions in time of detection. The distributions of the time (day of year means number of days from the start of 1996) of detection is plotted for **A**) Fe nuclei, and **B**) ^{60}Fe nuclei. The data set presented here begins on DOY96 704 and ends on DOY96 6845, corresponding to 4 December 1997 and 28 September 2014 respectively. The temporal variation of the number of counts is due to a combination of the solar-cycle variation of cosmic-ray modulation and to differences in the number of measurement days included in the various 200-day time bins. We have applied a Kolmogorov-Smirnov (K-S) statistical test to these distributions and obtain an asymptotic probability (p) of 0.13. Therefore the Fe and ^{60}Fe time distributions are not statistically different.

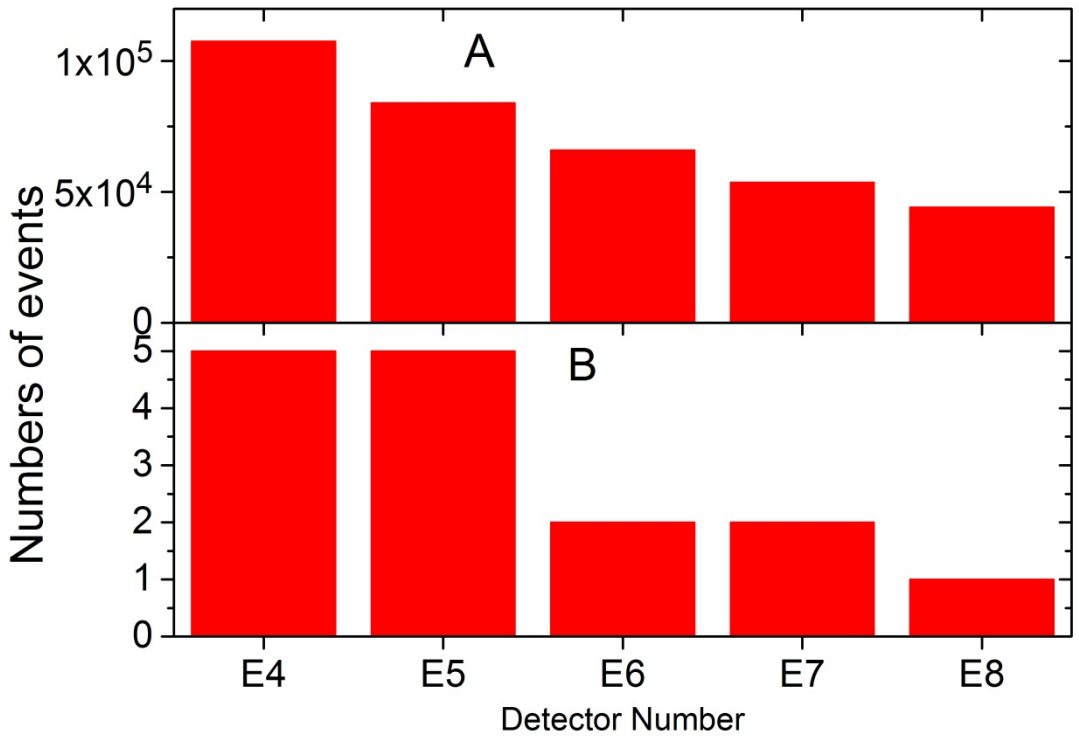

Fig. S4

Distributions in range. The number of events stopping in each of the detectors E4 through E8 is shown for **A**) Fe, and **B**) ^{60}Fe. The number of detectors used in the analysis is too small for a K-S statistical test to be valid. However, by inspection we see that the distributions are similar.

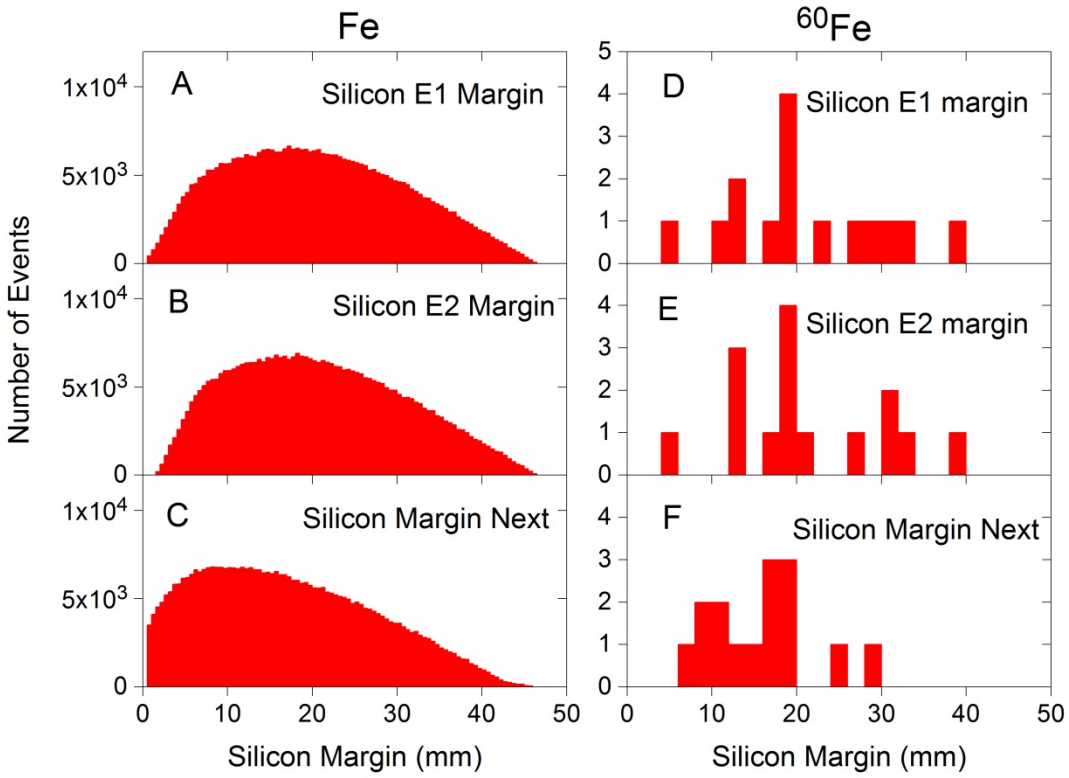

Fig. S5

Margin distributions in silicon detectors. The silicon detector margin distributions E1, E2, and Enext (see text) are shown in A, B, and C respectively for Fe and in D, E, and F respectively for ^{60}Fe. We have applied a Kolmogorov-Smirnov (K-S) statistical test to these distributions and obtain asymptotic probabilities (p) of 0.86, 0.87, and 0.24 respectively. Therefore the Fe and ^{60}Fe silicon margin distributions are not statistically different.

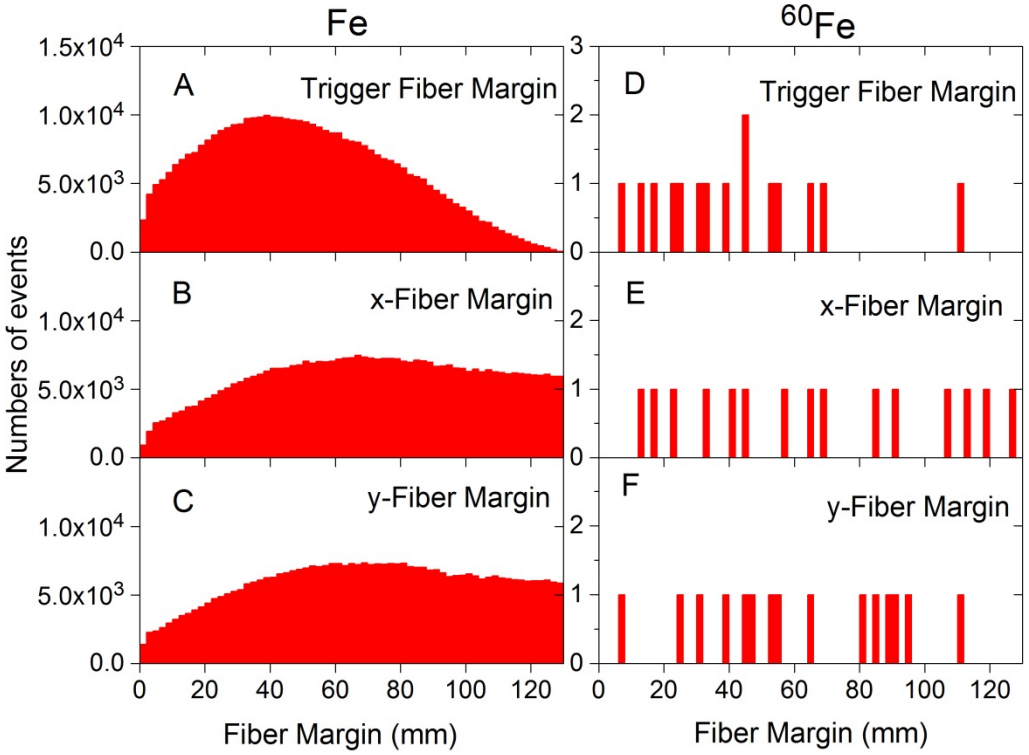

Fig. S6

Margin distributions in fiber hodoscope. The trigger fiber detector margin distributions "Trigger fiber margin", "x-fiber margin", and "y-fiber margin" (see text) are shown in A, B, and C respectively for Fe and in D, E, and F respectively for ^{60}Fe. We have applied a Kolmogorov-Smirnov (K-S) statistical test to these distributions and obtain asymptotic probabilities (p) of 0.33, 1.0, and 0.49 respectively. Therefore the Fe and ^{60}Fe fiber margin distributions are not statistically different.

References and Notes

1. G. Rugel, T. Faestermann, K. Knie, G. Korschinek, M. Poutivtsev, D. Schumann, N. Kivel, I. Günther-Leopold, R. Weinreich, M. Wohlmuther, New Measurement of the ^{60}Fe Half-Life. *Phys. Rev. Lett.* **103**, 072502 (2009). doi:10.1103/PhysRevLett.103.072502*http://www.nndc.bnl.gov/chart/* Medline

2. M. E. Wiedenbeck *et al*., Constraints on the time delay between nucleosynthesis and cosmic-ray acceleration from observations of ^{59}Ni and ^{59}Co. *Astrophys. J.* **523**, L61–L64 (1999). doi:10.1086/312242

3. S. E. Woosley, A. Heger, Nucleosynthesis and remnants in massive stars of solar metallicity. *Phys. Rep.* **442**, 269–283 (2007). doi:10.1016/j.physrep.2007.02.009

4. A. Chieffi, M. Limongi, Pre-supernova evolution of rotating solar metallicity stars in the mass range 13-120 $M_{\odot}$ and their explosive yields. *Astrophys. J.* **764**, 21 (2013). doi:10.1088/0004-637X/764/1/21

5. E. C. Stone, C. M. S. Cohen, W. R. Cook, A. C. Cummings, B. Gauld, B. Kecman, R. A. Leske, R. A. Mewaldt, M. R. Thayer, B. L. Dougherty, R. L. Grumm, B. D. Milliken, R. G. Radocinski, M. E. Wiedenbeck, E. R. Christian, S. Shuman, H. Trexel, T. T. von Rosenvinge, W. R. Binns, D. J. Crary, P. Dowkontt, J. Epstein, P. L. Hink, J. Klarmann, M. Lijowski, M. A. Olevitch, The cosmic-ray isotope spectrometer for the advanced composition explorer. *Space Sci. Rev.* **86**, 285–356 (1998). doi:10.1023/A:1005075813033

6. W. Wang, M. J. Harris, R. Diehl, H. Halloin, B. Cordier, A. W. Strong, K. Kretschmer, J. Knödlseder, P. Jean, G. G. Lichti, J. P. Roques, S. Schanne, A. von Kienlin, G. Weidenspointner, C. Wunderer, SPI observations of the diffuse ^{60}Fe emission in the Galaxy. *Astron. Astrophys.* **469**, 1005–1012 (2007). doi:10.1051/0004-6361:20066982

7. W. R. Binns, Cosmic-ray origins. *Science* **334**, 1071–1072 (2011). doi:10.1126/science.1213490 Medline

8. K. Knie, G. Korschinek, T. Faestermann, C. Wallner, J. Scholten, W. Hillebrandt, Indication for supernova produced ^{60}Fe activity on Earth. *Phys. Rev. Lett.* **83**, 18–21 (1999). doi:10.1103/PhysRevLett.83.18

9. K. Knie, G. Korschinek, T. Faestermann, E. A. Dorfi, G. Rugel, A. Wallner, ^{60}Fe anomaly in a deep-sea manganese crust and implications for a nearby supernova source. *Phys. Rev. Lett.* **93**, 171103 (2004). doi:10.1103/PhysRevLett.93.171103 Medline

10. C. Fitoussi, G. M. Raisbeck, K. Knie, G. Korschinek, T. Faestermann, S. Goriely, D. Lunney, M. Poutivtsev, G. Rugel, C. Waelbroeck, A. Wallner, Search for supernova-produced ^{60}Fe in a marine sediment. *Phys. Rev. Lett.* **101**, 121101 (2008). doi:10.1103/PhysRevLett.101.121101 Medline

11. B. J. Fry, B. D. Fields, J. R. Ellis, Astrophysical shrapnel: Discriminating among near-earth stellar explosion sources of live radioactive isotopes. *Astrophys. J.* **800**, 71 (2015). doi:10.1088/0004-637X/800/1/71

12. L. Fimiani *et al*., Sources of live ^{60}Fe, ^{10}Be, and ^{26}Al in lunar core 12025, core 15008, skim sample 69921, scoop sample 69941, and under-boulder sample 69961. *43rd Lunar and Planetary Science Conference*, 1279 (2012).

13. L. Fimiani *et al*., Evidence for deposition of interstellar material on the lunar surface. *45th Lunar and Planetary Science Conference*, 1778 (2014).

14. Materials and methods are available as supplementary materials on *Science* Online.

15. K. A. Lave, M. E. Wiedenbeck, W. R. Binns, E. R. Christian, A. C. Cummings, A. J. Davis, G. A. de Nolfo, M. H. Israel, R. A. Leske, R. A. Mewaldt, E. C. Stone, T. T. von Rosenvinge, Galactic cosmic-ray energy spectra and composition during the 2009-2010 solar minimum period. *Astrophys. J.* **770**, 117 (2013). doi:10.1088/0004-637X/770/2/117

16. J. C. Higdon, R. E. Lingenfelter, The superbubble origin of ^{22}Ne in cosmic rays. *Astrophys. J.* **590**, 822–832 (2003). doi:10.1086/375192

17. J. C. Higdon, R. E. Lingenfelter, OB associations, supernova-generated superbubbles, and the source of cosmic rays. *Astrophys. J.* **628**, 738–749 (2005). doi:10.1086/430814

18. N. E. Yanasak, M. E. Wiedenbeck, R. A. Mewaldt, A. J. Davis, A. C. Cummings, J. S. George, R. A. Leske, E. C. Stone, E. R. Christian, T. T. von Rosenvinge, W. R. Binns, P. L. Hink, M. H. Israel, Measurement of the secondary radionuclides ^{10}Be, ^{26}Al, ^{36}Cl, ^{54}Mn, and ^{14}C and implications for the galactic cosmic-ray age. *Astrophys. J.* **563**, 768–792 (2001). doi:10.1086/323842

19. P. T. de Zeeuw, R. Hoogerwerf, J. H. J. de Bruijne, A. G. A. Brown, A. Blaauw, A Hipparcos census of the nearby OB associations. *Astron. J.* **117**, 354–399 (1999). doi:10.1086/300682

20. R. Voss, R. Diehl, J. S. Vink, D. H. Hartmann, Probing the evolving massive star population in Orion with kinematic and radioactive tracers. *Astron. Astrophys.* **520**, A51 (2010). doi:10.1051/0004-6361/201014408

21. A. Wallner, J. Feige, N. Kinoshita, M. Paul, L. K. Fifield, R. Golser, M. Honda, U. Linnemann, H. Matsuzaki, S. Merchel, G. Rugel, S. G. Tims, P. Steier, T. Yamagata, S. R. Winkler, Recent near-Earth supernovae probed by global deposition of interstellar radioactive ^{60}Fe. *Nature* **532**, 69–72 (2016). doi:10.1038/nature17196

22. L. Fimiani, D. L. Cook, T. Faestermann, J. M. Gómez-Guzmán, K. Hain, G. Herzog, K. Knie, G. Korschinek, P. Ludwig, J. Park, R. C. Reedy, G. Rugel, Interstellar ^{60}Fe on the Surface of the Moon. *Phys. Rev. Lett.* **116**, 151104 (2016). doi:10.1103/PhysRevLett.116.151104

23. G. D. Westfall, L. W. Wilson, P. J. Lindstrom, H. J. Crawford, D. E. Greiner, H. H. Heckman, Fragmentation of relativistic ^{56}Fe. *Phys. Rev. C Nucl. Phys.* **19**, 1309–1323 (1979). doi:10.1103/PhysRevC.19.1309

24. L. A. Fisk, Solar modulation of galactic cosmic rays, 2. *J. Geophys. Res.* **76**, 221–226 (1971). doi:10.1029/JA076i001p00221

25. L. J. Gleeson, W. I. Axford, Solar modulation of galactic cosmic rays. *Astrophys. J.* **154**, 1011–1026 (1968). doi:10.1086/149822

26. E. E. Salpeter, The luminosity function and stellar evolution. *Astrophys. J.* **121**, 161–167 (1955). doi:10.1086/145971

27. J. M. Brown, S. E. Woosley, Nucleosynthetic constraints on the mass of the heaviest supernovae. *Astrophys. J.* **769**, 99 (2013). doi:10.1088/0004-637X/769/2/99

28. M. Limongi, A. Chieffi, The nucleosynthesis of ^{26}Al and ^{60}Fe in solar metallicity stars extending in mass from 11 to 120$M_{\odot}$: The hydrostatic and explosive contributions. *Astrophys. J.* **647**, 483–500 (2006). doi:10.1086/505164

29. C. Tur, A. Heger, S. M. Austin, Production of ^{26}Al, ^{44}Ti, and ^{60}Fe in core-collapse supernovae: Sensitivity to the rates of the triple alpha and $^{12}C(\alpha,\gamma)^{16}O$ reactions. *Astrophys. J.* **718**, 357 (2010). doi:10.1088/0004-637X/718/1/357

30. W. R. Binns, M. E. Wiedenbeck, M. Arnould, A. C. Cummings, J. S. George, S. Goriely, M. H. Israel, R. A. Leske, R. A. Mewaldt, G. Meynet, L. M. Scott, E. C. Stone, T. T. von Rosenvinge, Cosmic-ray neon, Wolf-Rayet stars, and the superbubble origin of galactic cosmic rays. *Astrophys. J.* **634**, 351–364 (2005). doi:10.1086/496959

31. B. F. Rauch, J. T. Link, K. Lodders, M. H. Israel, L. M. Barbier, W. R. Binns, E. R. Christian, J. R. Cummings, G. A. de Nolfo, S. Geier, R. A. Mewaldt, J. W. Mitchell, S. M. Schindler, L. M. Scott, E. C. Stone, R. E. Streitmatter, C. J. Waddington, M. E. Wiedenbeck, Cosmic ray origin in OB associations and preferential acceleration of refractory elements: Evidence from abundances of elements $_{26}$Fe through $_{34}$Se. *Astrophys. J.* **697**, 2083–2088 (2009). doi:10.1088/0004-637X/697/2/2083

32. W. R. Binns *et al*., Constraints on galactic cosmic-ray origins from elemental and isotopic composition measurements. Proc. 33rd Intl. Cosmic Ray Conference (Rio de Janeiro), Paper 646 (2013). http://www.cbpf.br/~icrc2013/papers/icrc2013-0646.pdf

33. R. P. Murphy, Identifying the origin of galactic cosmic rays with the SuperTIGER instrument. *PhD Thesis*, Washington University in St. Louis (2015). http://openscholarship.wustl.edu/art_sci_etds/670/